Abrahamson and K. Shedlock, *Seismol. Rev. Lett.* **68**, 9 (1997).
9. R. Whirley *et al.*, *DYNA2D: A Nonlinear, Explicit, Two-Dimensional Finite Element Code for Solid Mechanics—User Manual* (UCRL-MA-110630, University of California, Lawrence Livermore National Laboratory, Livermore, CA, 1992).
10. D. Andrews, *J. Geophys. Res.* **81**, 3575 (1976); *ibid.*, p. 5679; R. Archuleta, thesis, University of California, San Diego (1976); ——— and P. Frazier, *Bull. Seismol. Soc. Am.* **68**, 541 (1978); S. Day, *ibid.* **72**, 705 (1982); *ibid.*, p. 1881; A. Ruina, *J. Geophys. Res.* **88**, 10359 (1983); T. Mikumo and T. Miyatake, *Geophys. J. Int.* **112**, 481 (1993); R. Madariaga and A. Cochard, *Proc. Natl. Acad. Sci. U.S.A.* **93**, 3819 (1996).
11. Stresses in this report are defined according to Fig. 1. σ_x and σ_y are the normal stresses in the x and y directions; σ_n is the normal stress across the fault; σ_{xy} and σ_{yx} are the shear stresses in the x and y directions; τ is the (frictional) shear stress along the fault. The yield stress level is equal to $\mu\sigma_n$ where μ is the static frictional coefficient. The sliding frictional stress level is equal to $\mu'\sigma_n$, where μ' is the sliding frictional coefficient.
12. The stress drop is a cosine function from with a drop time of 0.2 s. This form corresponds to a slip-weakening friction law, with an effective slip-weakening distance (*15*) of 1 to 20 cm, depending on the slip rate.
13. We derive a general solution for the change in rupture criterion in a manner analogous to that of S. Nielsen [*Geophys. Rev. Lett.* **25**, 125 (1998)].
14. The stress field in the vicinity of a slip-weakening crack has been explored [Y. Ida, *J. Geophys. Res.* **77**, 3796 (1972); D. Andrews, *ibid.* **81**, 5679 (1976)].
15. J. Rudniki and M. Wu, *ibid.* **100**, 22173 (1995).
16. Breakout phases (large radiation pulses emitted when the rupture front breaks through the free surface) are examined in R. Burridge and G. Halliday, *Geophys. J. R. Astron. Soc.* **25**, 261 (1971).
17. B. J. Shi *et al.*, in preparation.
18. P. Davis and L. Knopoff, *Geophys. J. Int.* **106**, 581 (1991).
19. This may be an indication that our friction law or healing criterion, or both, may not be valid right at the free surface.
20. The seismic moment [K. Aki, *Bull. Earthquake Res. Inst. Tokyo Univ.* **44**, 73 (1966)] is the standard measurement for the absolute size of an earthquake and is defined as $M_0 = \mu\bar{s}A$, where μ is the shear modulus, $\bar{s}$ is the average slip on the fault, and A is the area on the fault in which slip occurred.
21. Examples of aftershock locations are seen in the 1983 Coalinga, California, earthquake; the 1981 Corinth, Greece, earthquake; the 1980 El Asnam, Algeria, earthquake; the 1982 Miramichi, Canada, earthquake [D. Eberhart-Phillips and P. Reasenberg, in *The Coalinga, California, Earthquake of May 2, 1983*, M. Rymer and W. Ellsworth, Eds., *U.S. Geol. Surv. Prof. Pap.* **1487**, 171 (1990)]; and the 1994 Northridge earthquake [H. Thio and H. Kanamori, *Bull Seismol. Soc. Am.* **86**, S84 (1996)].
22. Y. Zeng, personal communication; R. Sibson, personal communication.
23. Fault friction and weakness are discussed in detail in C. Scholz, *The Mechanics of Earthquakes and Faulting* (Cambridge Univ. Press, Cambridge, 1989), pp. 44–91.
24. J. Byerlee, *Pure Appl. Geophys.* **116**, 615 (1978).
25. Computations for this study were carried out primarily on the SGI Origin 2000 at the Materials Research Laboratory, University of California, Santa Barbara (UCSB) (NSF grant CDA96-01954). This research was supported by UCSB, UCSB/Campus Laboratory Collaboration grant 08950868, and Lawrence Livermore National Laboratory–Institute of Geophysics and Planetary Physics grant 98-GS012. S.B.N. was supported by the Materials Research Science and Engineering Center Program of the NSF under award DMR96-32716. This work is Institute for Crustal Studies contribution 0286-69EQ. The authors gratefully acknowledge the extensive programming advice of E. Zywicz and the support and advice of W. Foxall and L. Hutchings.

17 November 1997; accepted 18 March 1998

Percolation of Core Melts at Lower Mantle Conditions

M. C. Shannon and C. B. Agee

Experiments at high pressure and temperature to determine the dihedral angle of core melts in lower mantle phases yielded a value of ~71° for perovskite-dominated matrices. This angle, although greater than the 60° required for completely efficient percolation, is considerably less than the angles observed in mineral matrices at upper mantle pressure-temperature conditions in experiments. In other words, molten iron alloy can flow much more easily in lower mantle mineralogies than in upper mantle mineralogies. Accordingly, although segregation of core material by melt percolation is probably not feasible in the upper mantle, core formation by percolation may be possible in the lower mantle.

Core formation is by far the largest mass transfer event in Earth history. For a homogeneous chondritic Earth this event involves the separation of iron metal from silicate material to form a metallic core with an overlying silicate mantle. Two possible separation mechanisms have emerged (*1*): melt segregation through a molten matrix, a process commonly referred to as rainfall, and melt segregation through a solid matrix, usually termed percolation. Rainfall requires that some or all of the silicate mantle was molten, allowing the molten iron droplets to "fall" to the center as a result of their greater density. Percolation involves molten iron moving through solid rock by flowing between grains along an interconnected grain-edge pore network. Several experimental studies showed that percolation in the upper mantle would not be possible (*2–4*). The fluid-solid interfacial energy of molten iron and iron-sulfur alloys in lower mantle aggregates is too high, relative to the grain boundary energies of a rock matrix of olivine (and its higher pressure polymorphs), pyroxene, and garnet, to permit the melts to form an interconnected network. Percolation is therefore inefficient, stranding some of the metallic alloy in the silicate matrix. Because rock samples from the upper mantle show no evidence of stranded core material, true percolation is ruled out. In the lower mantle, however, the mineralogy changes to a matrix dominated by (Mg, Fe)SiO_3 perovskite and magnesiowuestite (*5*). The physical properties of perovskite and magnesiowuestite differ from those of olivine and pyroxene because of the coordination change of silicon from tetrahedral (coordinated to four oxygen atoms) to octahedral (coordinated to six oxygen atoms). It is unknown how iron alloy interacts with these lower mantle phases, although an enhanced percolation ability is suspected (*1*, *6*). Here we examined the ability of iron alloy to form an interconnected grain-edge network with perovskite and magnesiowuestite.

Department of Earth and Planetary Sciences, Harvard University, Cambridge, MA 02138, USA.

Experiments were performed with a multi-anvil device; the experimental setup was similar to that described in (*7*) except that a carbon capsule was used to separate the starting material from the heater and no thermocouple was present. Temperature was estimated on the basis of power consumption and a comparison of textures from similar experiments run with a thermocouple (*8*). We used two starting materials: Homestead meteorite (an L5 ordinary chondrite) and a mixture of enstatite and iron sulfide. Both starting materials were ground to an average grain size of 5 to 10 μm. The materials were pressurized to ~25 GPa and heated to a point just below the silicate solidus where the silicates and oxides are solid and the iron alloy is molten, about 2100°C. These conditions were maintained for 3 hours to achieve a close approximation to textural equilibrium. In the 25-GPa runs, the original phases of Homestead recrystallized to form perovskite $(Mg_{.76}Fe_{.24})SiO_3$, magnesiowuestite $(Mg_{.35}Fe_{.65})O$, garnet, calcium perovskite, and quenched iron-nickel-sulfur melt $(Fe_{81}Ni_7S_{12})$ (Fig. 1A). The original enstatite recrystallized to form perovskite $(Mg_{.95}Fe_{.05})SiO_3$ in contact with quenched iron-sulfide melt $(Fe_{89}Ni_1S_{10})$ (Fig. 1B).

To characterize percolation ability, we determined the dihedral angle that the quenched alloy (molten during run conditions) forms with the solid silicate phases from the polished sections. Because the dihedral angle is measured in the plane normal to the axis of the triple junction between two solid grains and a quenched melt pocket, measured angles in a single section will produce a distribution of apparent angles (*9*). We approximate the true angle with the median of the distribution of apparent angles (*10*). A dihedral angle of 60° or less indicates that efficient percolation is possible. A value greater than 60° implies that some melt will be stranded, with the amount of melt stranded increasing with increasing angle (*11–13*). All three distributions show broadening relative to the theoretically expected distribution characteristic of matrices with nonisotropic phases (*9, 10, 14*). In addition, the broad distribution of the Homestead experiment (Fig. 2A) results from contact between several different solid phases and melt. The distribution of angles is narrower for contacts measured between only perovskite and the alloy (Fig. 2B).

Another possible explanation for the broad peaks is that the textures are not in equilibrium. In that case, the median may not be a good approximation for the dihedral angle. However, we suggest that these textures are in equilibrium for three reasons. Previous studies have shown that at elevated pressures and temperatures, the dihedral angle does not change significantly after a few hours of run time (*3, 4*). Second, the results from preliminary experiments run for 5 to 60 min or at lower temperatures give bimodal distributions or broad peaks (*15*). The relatively narrow, single peaks of the two experiments here show that the dihedral angle is approaching a single value. Finally, a quantitative analysis of the angles formed at triple junctions of perovskite grains shows that the perovskite matrix that forms the bulk of the sample has reached an equilibrium texture (*16*). Therefore, we are confident that, within error, the median of the apparent distribution is representative of the dihedral angle.

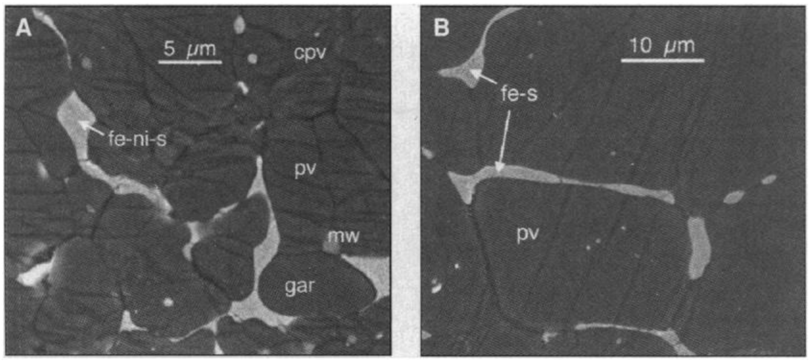

Fig. 1. (**A**) Results for the Homestead meteorite starting composition (run 760), run at ~25 GPa and ~2100°C. The matrix is dominated by perovskite (pv) with grains of magnesiowuestite (mw), garnet (gar), calcium perovskite (cpv), and pockets of quenched iron-nickel-sulfur melt (fe-ni-s). (**B**) Results for the enstatite starting composition (run 762), obtained under the same conditions as run 760. The matrix is entirely magnesium-rich perovskite (pv) with pockets of quenched iron-sulfur melt (fe-s).

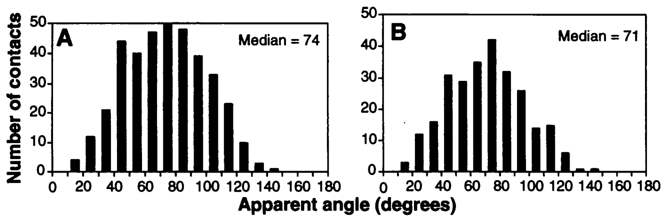

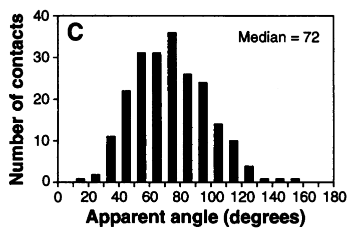

Fig. 2. (**A**) Distribution of apparent dihedral angles for all phases formed from the Homestead meteorite starting composition. The number of contacts measured was 375. This peak is broader than the peaks in (B) and (C) because of the presence of magnesiowuestite, garnet, and calcium perovskite in addition to the perovskite in the matrix. (**B**) Distribution of apparent dihedral angles for contacts between iron-alloy melt and perovskite formed from the Homestead meteorite starting composition. The number of contacts measured was 263. (**C**) Distribution of apparent dihedral angles for contacts between iron-alloy melt and perovskite formed from the enstatite starting composition. The number of contacts measured was 215.

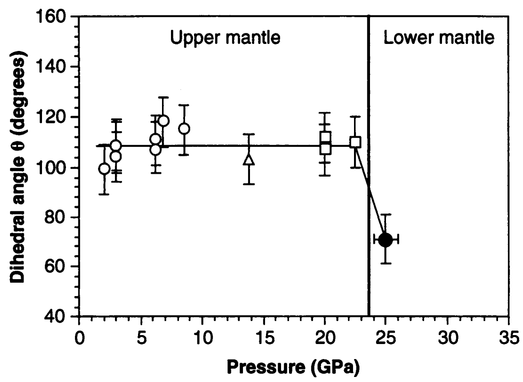

Fig. 3. Dihedral angle versus pressure diagram for the Homestead L5 chondrite. The plotted value of dihedral angle θ is the median angle of a distribution of apparent angles; error bars are ±10°. Open symbols represent upper mantle phases (circle, olivine; triangle, β-phase; square, γ-spinel), which all yield a dihedral angle of ~108°, from (*4*); the filled circle represents run 760 from this study. The point at 23.5 GPa was run in the same setup as the runs in this study and is a "bridge" to our previous results. γ-Spinel, perovskite, and magnesiowuestite were all stable in the charge; however, only angles at junctions with γ-spinel were measurable.

Both the iron-bearing perovskite (Homestead sample) and the magnesium-rich perovskite (enstatite sample) produced a dihedral angle of ~71° (Fig. 2), suggesting that the iron content of the perovskite has no effect on the percolation ability of the melt. The value of 74° produced by the entire Homestead matrix (Fig. 2A) agrees with the perovskite values and reflects the dominance of perovskite in the solid matrix of this meteorite. The other solid phases present, magnesiowuestite, garnet, and calcium perovskite, were not abundant enough to yield distinct dihedral angle measurements or change the percolation ability of the melt (*17*). The decrease in the dihedral angle to 71° from the 108° value measured for the Homestead meteorite composition at upper mantle conditions (Fig. 3) (*4*) indicates a change in the interfacial energies of the solid phases when the minerals γ-spinel and pyroxene transform to perovskite and magnesiowuestite. Such a shift does not occur at lower pressures when olivine transforms to β-phase and γ-spinel and may in part be due to a change in atomic packing.

The reduction in dihedral angle indicates a change in the percolative ability of the melt. In experiments simulating upper mantle matrices, the larger dihedral angle indicates that the fraction of melt that will be stranded is at least 6 to 10% by volume of the sample (*12, 13, 18*). The lower dihedral angle measured here in experiments simulating lower mantle matrices indicates that the stranded melt fraction will be smaller, although how much smaller is not precisely known. For a melt forming a dihedral angle of 71° with a monomineralic isotropic matrix, the stranded melt fraction is about 2.5 to 3% (*13*). When the solid phase or phases are anisotropic, as perovskite is, the fraction of melt stranded has been shown to be higher (*19*).

Changes in pressure, temperature, and composition with depth can also change the dihedral angle. Previous work has shown that, in similar systems, dihedral angle decreases with increasing temperature (*2, 20*). At the same time, increasing pressure may increase dihedral angle (*3, 4*). Melt composition also has an influence (*2, 3*). The profile of dihedral angle throughout the lower mantle then will depend on the interaction of all of these factors as the pressure and temperature increase. Better constraints on the effects of pressure, temperature, and composition are needed before the percolative ability of the lower mantle can be completely assessed; however, the ~35° decrease in dihedral angle due to the mineralogy change at the upper-lower mantle boundary suggests percolation in the lower mantle may be a feasible core segregation mechanism.

For the early Earth, these results are most relevant to models of core formation. Core formation by percolation in the entire mantle is not feasible because of the large dihedral angle in matrices formed at lower pressures. Some melting of the silicates, diapiric instability, or a nonequilibrium process such as shearing may have been required to mobilize the melt downward at lower pressures. However, the decrease in dihedral angle in lower mantle assemblages suggests that percolation in the deep Earth may be possible under some conditions. If so, then core formation could have proceeded by rainfall through melted silicates at lower pressures (<25 to 30 GPa) (*21*) and by percolation at greater pressures. If percolation is not enough enhanced by the decrease in dihedral angle to allow complete segregation of core material, then other mechanisms to mobilize the melt such as partial melting of silicates or shearing are needed to complete core formation.

These data also have ramifications for Earth now. The ability of core material to infiltrate the lower mantle at the core-mantle boundary is also characterized, in part, by the dihedral angle. An angle on the order of 71° means that core melt could percolate upward, by capillary action, some distance into the base of the lower mantle. The density contrast between mantle and core may allow only a thin zone of metal capillary infiltration. If molten iron is entrained in D″, then it will tend to percolate back to the core along grain boundary pathways. The amount of melt present and the distance of infiltration will provide important constraints on models of the formation of D″, interactions at the core mantle boundary, and mantle dynamics (*22*).

REFERENCES AND NOTES

1. D. J. Stevenson, in *Origin of the Earth*, J. E. Newsom and J. H. Jones, Eds. (Oxford Univ. Press, New York, 1990), pp. 231–249.
2. C. Ballhaus and D. J. Ellis, *Earth Planet. Sci. Lett.* **143**, 137 (1996).
3. W. G. Minarik, F. J. Ryerson, E. B. Watson, *Science* **272**, 530 (1996).
4. M. C. Shannon and C. B. Agee, *Geophys. Res. Lett.* **23**, 2717 (1996).
5. E. Ito and E. Takahashi, *J. Geophys. Res.* **94**, 637 (1989).
6. F. Goarant *et al.*, *ibid.* **97**, 4477 (1992); S. Urakawa, M. Kato, M. Kumazawa, in *High-Pressure Research in Mineral Physics*, M. H. Manghnani and Y. Syono, Eds. (American Geophysical Union, Washington, DC, 1987), pp. 95–111.
7. C. B. Agee, J. Li, M. C. Shannon, S. Circone, *J. Geophys. Res.* **100**, 17725 (1995).
8. Experiments run in the same setup with a thermocouple include the following: [run number, starting material, pressure (GPa), temperature (°C), and duration (minutes)]: 579, Homestead, 23, 2000, 2; 632, Homestead, 23, 1750, 60; 714, Homestead, 24.5, 1760, 180; 719, Homestead, 24.5, 1900, 210; and enstatite + Fe + S, 24.5, 1900, 210. Pressures are to within ±1 GPa, temperatures have been corrected from TC reading to account for the difference in temperature inside and outside the capsule and are to within ±100°C.
9. C. S. Smith, *Metall. Rev.* **9**, 1 (1964).
10. S. R. Jurewicz and A. J. G. Jurewicz, *J. Geophys. Res.* **91**, 9277 (1986).
11. P. J. Wray, *Acta Metall.* **24**, 125 (1976).
12. J. R. Bulau, H. S. Waff, J. A. Tyburczy, *J. Geophys. Res.* **84**, 6102 (1979).
13. N. von Bargen and H. S. Waff, *ibid.* **91**, 9261 (1986).
14. C. A. Stickels and E. E. Hucke, *Trans Metall. Soc. AIME* **230**, 795 (1964).
15. Experiments used for comparison include those listed in (*8*) plus three others: 559, Homestead, 25, 2100, 2; 636, Homestead, 24.5, 1900, 60; and 756, Homestead, 25, 2200, 180.
16. M. T. Elliott, M. J. Cheadle, D. A. Jerram, *Geology* **25**, 355 (1997).
17. Angles formed by quenched melt in contact with perovskite and another solid phase were abundant enough to characterize. Medians for these types of contacts were 78 (24 contacts) for perovskite + magnesiowuestite; 93 (45 contacts) for perovskite + calcium perovskite, and 60 (35 contacts) for perovskite + garnet.
18. S. R. Jurewicz and J. H. Jones, *Proc. Lunar Planet. Sci.* **XXVI**, 709 (1995).
19. U. H. Faul, *J. Geophys. Res.* **102**, 10299 (1997); D. Laporte and E. B. Watson, *Chem. Geol.* **124**, 161 (1995).
20. M. A. Herpfer, thesis, Arizona State University (1992).
21. J. Li and C. B. Agee, *Nature* **381**, 686 (1996); K. Righter, M. J. Drake, G. Yaxley, *Phys. Earth Planet. Int.* **100**, 115 (1997).
22. M. Manga and R. Jeanloz, *Geophys. Res. Lett.* **23**, 3091 (1996).

23. We thank three anonymous reviewers for helpful comments. Supported by NSF.

10 October 1997; accepted 31 March 1998

Localized Reconnection in the Near Jovian Magnetotail

C. T. Russell,* K. K. Khurana, D. E. Huddleston, M. G. Kivelson

The oppositely directed magnetic field in the jovian magnetic tail is expected eventually to reconnect across the current sheet, allowing plasma produced deep inside the magnetosphere near Io's orbit to escape in the antisolar direction down the tail. The Galileo spacecraft found localized regions of strong northward and southward field components beyond about 50 jovian radii in the postmidnight, predawn sector of the jovian magnetosphere. These pockets of vertical magnetic fields can be stronger than the surrounding magnetotail and magnetodisk fields. They may result from episodic reconnection of patches of the near jovian magnetotail.

The Galileo spacecraft has, since insertion on 7 December 1995, operated at Jupiter in a series of orbits whose line of apsides has rotated from a position behind the dawn terminator to close to midnight. The eighth of these orbits had sufficient telemetry bandwidth that nearly continuous measurements could be obtained through the apojove region and telemetered to Earth. This allowed us to study the temporal stability of the magnetodisk and near magnetotail with the data from the magnetometer (*1*) from midnight to 3 AM local time and at distances from 50 to 100 jovian radii (R_J) from the planet (Fig. 1A). On the basis of previous observations by Pioneer 10 and 11 (*2*), Voyager 1 and 2 (*3*), and Ulysses (*4*), we expected the magnetospheric field to be radially directed through most of this region except near the current sheet. The tilt of the magnetic dipole axis controls the current sheet location so that the current sheet is, in general, displaced from the rotational equator in which Galileo orbits so that it can fly by the four Galilean moons (Fig. 1B). The rotation of Jupiter carries the current sheet back and forth across Galileo every 10 hours.

The volcanic moon Io supplies up to a ton of ions per second to the jovian magnetosphere. This material is transported radially outward to ultimately be lost down the tail in the antisolar direction (*5, 6*). In a perfectly electrically conducting fluid, the

C. T. Russell and M. G. Kivelson, Institute of Geophysics and Planetary Physics, and Department of Earth and Space Sciences, University of California, Los Angeles, CA 90095-1567, USA.
K. K. Khurana and D. E. Huddleston, Institute of Geophysics and Planetary Physics, University of California, Los Angeles, CA 90095-1567, USA.

*To whom correspondence should be addressed. E-mail: ctrussell@igpp.ucla.edu